AGU PUBLICATIONS

Water Resources Research

RESEARCH ARTICLE
10.1002/2015WR018072

Imaging of oil layers, curvature and contact angle in a mixed-wet and a water-wet carbonate rock

Kamaljit Singh[1], Branko Bijeljic[1], and Martin J. Blunt[1]

[1]Qatar Carbonates and Carbon Storage Research Centre, Department of Earth Science and Engineering, Imperial College London, London, UK

Key Points:
- Mixed-wet conditions were obtained by chemical treatment of the carbonate rock
- X-ray micro-tomography was used to resolve oil layers in oil-wet pores and throats
- In situ contact angle, brine-oil curvatures and local capillary pressure were measured

Correspondence to:
K. Singh,
kamaljit.singh@imperial.ac.uk

Citation:
Singh, K., B. Bijeljic, and M. J. Blunt (2016), Imaging of oil layers, curvature and contact angle in a mixed-wet and a water-wet carbonate rock, *Water Resour. Res.*, *52*, doi:10.1002/2015WR018072.

Received 5 SEP 2015
Accepted 7 FEB 2016
Accepted article online 12 FEB 2016

Abstract We have investigated the effect of wettability of carbonate rocks on the morphologies of remaining oil after sequential oil and brine injection in a capillary-dominated flow regime at elevated pressure. The wettability of Ketton limestone was altered in situ using an oil phase doped with fatty acid which produced mixed-wet conditions (the contact angle where oil contacted the solid surface, measured directly from the images, $\theta = 180°$, while brine-filled regions remained water-wet), whereas the untreated rock (without doped oil) was weakly water-wet ($\theta = 47 \pm 9°$). Using X-ray micro-tomography, we show that the brine displaces oil in larger pores during brine injection in the mixed-wet system, leaving oil layers in the pore corners or sandwiched between two brine interfaces. These oil layers, with an average thickness of 47 ± 17 μm, may provide a conductive flow path for slow oil drainage. In contrast, the oil fragments into isolated oil clusters/ganglia during brine injection under water-wet conditions. Although the remaining oil saturation in a water-wet system is about a factor of two larger than that obtained in the mixed-wet rock, the measured brine-oil interfacial area of the disconnected ganglia is a factor of three smaller than that of oil layers.

1. Introduction

Two-phase flow in porous media is a complex pore-scale phenomenon, which has many applications including oil recovery from reservoirs, subsurface nonaqueous phase liquid (NAPL) contaminant transport and remediation, and effective geo-sequestration of CO_2 to address global warming [*Honeyman*, 1999; *Shaffer*, 2010; *Morrow and Buckley*, 2011]. Wettability, characterized by the contact angle at the three-phase contact line, is a key parameter that controls the flow pattern and pore-scale dynamics of immiscible displacement [*Cieplak and Robbins*, 1988, 1990; *Trojer et al*., 2015]. In a water-wet porous medium, water flows through smaller pores and corners leaving behind a fraction of oil ganglia in the centers of larger pores held in place by strong capillary forces [*Chatzis et al*., 1983; *Schnaar and Brusseau*, 2005; *Al-Raoush*, 2009; *Singh et al*., 2011; *Iglauer et al*., 2012]. The trapped nonwetting phase ganglia can occupy one to many pores, with a power-law distribution of size, consistent with percolation theory [*Iglauer et al*., 2010, 2012; *Andrew et al*., 2014a].

Most reservoir rocks are likely to have an altered wettability due to the deposition of asphaltene on solid surfaces exposed to crude oil [*Kovscek et al*., 1993]. During primary oil migration, oil invades the wider pore spaces. Where the oil directly contacts the surface, these surfaces may become oil-wet. Smaller pores and the corners of the pore space remain water-filled and water-wet, creating what we term here a mixed-wet system. When water is injected into the pore space to displace oil, oil layers may form, sandwiched between water in the water-wet corners of the pore space and water occupying the centers. Oil recovery under these mixed-wet conditions has been reported to increase with increasing number of pore volumes of brine injection, due to slow drainage through these layers [*Salathiel*, 1973]. This is in contrast to a water-wet system in which most of the oil is recovered up to water breakthrough.

The advent of pore-scale imaging using X-ray micro-tomography has allowed fluid configurations to be seen directly in rock samples. Imaging has been applied to the study of dynamic displacement [*Berg et al*., 2013; *Andrew et al*., 2015] and water flooding in a complex carbonate rock [*Pak et al*., 2015]. For a recent review on this imaging technique for immiscible fluid flow in porous media, refer to *Wildenschild and Sheppard* [2013]. Most of the available literature has focused on imaging two-phase flow in water-wet porous media, and only a few studies have been conducted under mixed-wet conditions. Although layer flow in a

mixed-wet system has been predicted and used in many theoretical and simulation studies [*Blunt*, 1997, 2001; *Valvatne and Blunt*, 2004; *Piri and Blunt*, 2005; *van Dijke and Sorbie*, 2006; *Ryazanov et al*., 2010], it has not been experimentally investigated and visualized in realistic three-dimensional porous media. Here, layer flow refers to the flow of oil through connected oil layers that are sandwiched between water in the center of the pore space and water in the corners [*Kovscek et al*., 1993; *Blunt*, 1997]. An indication of oil-spreading layers for a three-phase (water-oil-gas) fluid system has been observed in a sandstone using a high attenuating oil phase [*Feali et al*., 2012].

There are three studies which have used X-ray micro-tomography to investigate residual oil in fractionally wet and oil-wet media at ambient conditions [*Al-Raoush*, 2009; *Kumar et al*., 2010; *Iglauer et al*., 2012]; however, the wettability and contact angle of these systems were not well defined. The wettability was altered either by chemically treating the sand and then mixing the treated and the untreated sand particles to create fractionally wet porous media [*Al-Raoush*, 2009], by ageing sandstone rock samples with crude oil [*Iglauer et al*., 2012] or by creating patched wetting conditions by freezing the initial water and chemically treating the rest of the core [*Kumar et al*., 2010]. *Al-Raoush* [2009] and *Iglauer et al*. [2012] have reported a lower oil saturation in a fractionally wet and a mixed-wet porous medium after water flooding compared to that in a water-wet porous medium, however, *Kumar et al*. [2010] reported a slightly higher value of residual oil for patched wettability. These contrary observations clearly show gaps in the available literature; therefore further studies are needed to be conducted under controlled experimental conditions to understand the behavior of two-phase flow in mixed-wet porous media.

In this work, we use X-ray micro-tomography to conduct in situ experiments on the entrapment of oil and oil layer formation as a function of wettability. We demonstrate the existence of pore-scale oil layers in a mixed-wet carbonate rock at reservoir pressure and ambient temperature. Firstly, we describe the experimental procedure for creating both water-wet and mixed-wet systems: we dope the oil with fatty acids which render the solid surfaces in contact with oil strongly oil-wet. We then perform oil flood and brine flood experiments to compare images of fluid distributions acquired under mixed-wet conditions with an untreated, water-wet system. We analyze oil morphologies, interfacial curvatures, contact angles, brine-oil interfacial area and residual/remaining oil saturation and show that substantial differences in these parameters exist between the two wettabilities. For mixed-wet systems, we perform throat invasion analysis in both oil and brine flooding, and relate the fluid occupancy to the throat size.

2. Materials and Methods

2.1. Materials

The experiments were conducted on 5 mm diameter and 25 mm long Ketton limestone rock samples from the Ketton quarry, Rutland, UK, which contains $>$99% calcite [*Andrew et al*., 2014b]. These samples were cleaned with methanol using Soxhlet extraction apparatus for 24 h, followed by drying in a vacuum oven at 100°C for 24 h. A solution of 7 wt% potassium iodide (KI) salt (puriss, 99.5%, Sigma-Aldrich, U.K) in deionized water was used as aqueous phase, which provided an effective contrast between brine, oil and rock phases. Decane (ReagentPlus, $\geq$99%, Sigma-Aldrich, U.K.) and 0.01 M solution of stearic acid (Grade I, $\geq$98.5%, Sigma-Aldrich, U.K.) in decane (hereafter called doped-decane) was used as the oil phase for water-wet and mixed-wet systems respectively. Decane was filtered four times through a column of aluminum oxide powder to remove surface active impurities and to obtain a stable brine-oil interfacial tension [*Goebel and Lunkenheimer*, 1997].

The interfacial tension between brine-decane and brine-doped decane was measured to be 40.38 ± 0.12 mN/m and 13.41 ± 0.14 mN/m respectively at 21.9°C using the pendant drop method [*Andreas et al*., 1937; *Stauffer*, 1965]. The density of brine and decane was measured to be 1052.1 ± 2.2 kg/m^3 and 726.5 ± 1.2 kg/m^3 respectively at 22°C.

2.2. Experimental Method

2.2.1. Sample Preparation and Core Saturation

The flow loop of the apparatus is shown in Figure 1. The experiments were conducted in a Hassler type flow cell made of carbon fiber that is nearly transparent to X-rays [*Andrew et al*., 2014a]. The cylindrical sample was placed in a Viton sleeve which was attached to metal end pieces on both sides of the sample.

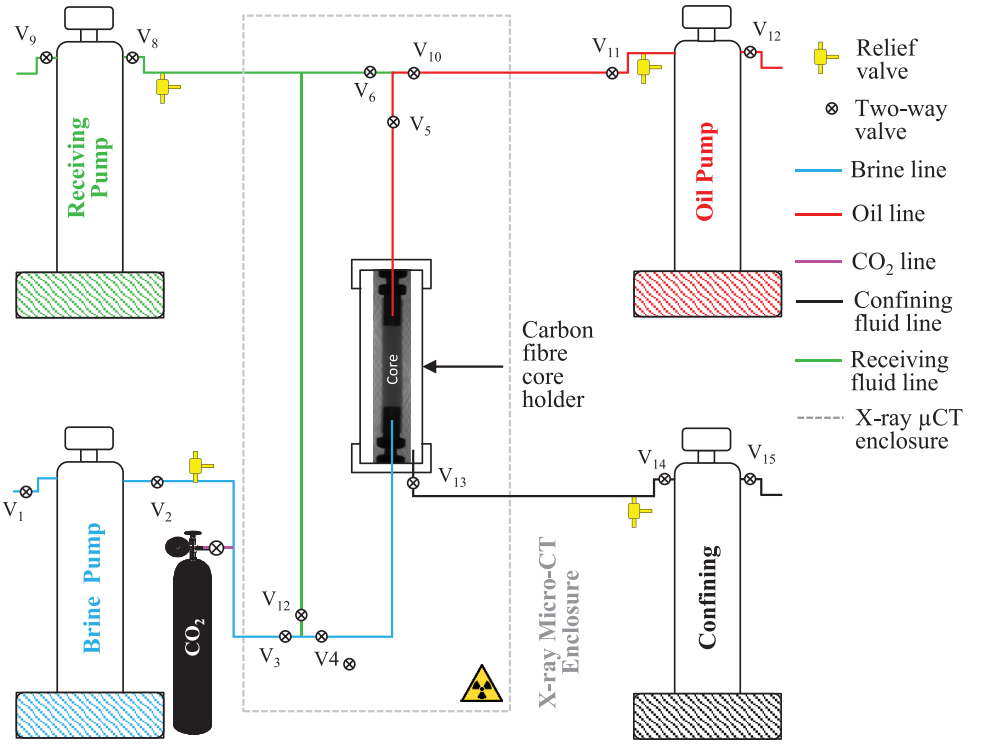

Figure 1. Experimental apparatus. Oil and brine pumps were used for maintaining fluid pressure (10 MPa) during oil and brine injection respectively, while the receiving pump was used to pull the liquids through the core at a constant flow rate of 15 μL/min. The confining pump maintained a pressure of 11.2 MPa confining the Viton sleeve in which the sample was mounted.

The metal end pieces were fitted to PEEK tubes making a flow loop with brine and oil injection pumps along with a receiving pump. After loading the sample, the rock was flushed with CO_2 to displace air followed by 80–100 pore volumes (PV) of brine injection at 0.1–0.2 mL/min to remove CO_2 dissolved brine, ensuring 100% brine saturation. The pressure in the brine and the confining fluid (deionized water) was then raised to 10 MPa and 11.2 MPa respectively. A higher confining pressure was used to confine the Viton sleeve in which the sample was mounted to avoid any fluid bypassing along the walls of the rock sample.

2.2.2. Oil Injection (Drainage)

During oil flooding, the oil pump maintained the pressure of the system (10 MPa), while the receiving pump pulled the oil through the core at a constant flow rate of 15 μL/min corresponding to a macroscopic capillary number ($N_c = v\mu/\sigma$, where v is the average velocity of the invading fluid, μ is the viscosity of the invading fluid and σ is the brine-oil interfacial tension) of 2.2×10^{-7} and 7.6×10^{-7} for decane and doped-decane respectively, representing a capillary-dominated flow regime. A total of 14–20 pore volumes of oil were injected. The rock sample was then imaged with a voxel size of 6.4 μm at 2–3 vertical locations (which were then stitched together for a larger image) using a Zeiss Xradia 500 Versa 3D X-ray microscope with 80–100 kV and 7–9 W settings. All the experiments were conducted at ambient temperature (20°C).

2.2.3. Rock Ageing for Mixed-Wet Conditions

In the case of the doped-decane after oil injection, the system was left overnight (12–16 h) for ageing to alter the wettability of the oil-filled pore spaces. The change in wettability occurs due to the attraction of negatively charged tail of stearic acid in decane to the positively charged calcium ions, forming a layer of calcium stearate that offers strong oil-wet conditions [*Hansen et al.*, 2000; *Hamouda and Rezaei Gomari*, 2006]. This treatment provides us with a mixed-wet system with the larger oil-invaded pores becoming oil-wet, while smaller pore spaces and the corners remain water-wet.

2.2.4. Brine Injection

During brine injection, the flow was reversed for both experiments (i.e., decane and doped-decane), the brine was supplied from the base for 18.5–19 PV at a constant flow rate of 15 μL/min corresponding to a macroscopic capillary number of 1.7×10^{-7} and 6.1×10^{-7} for decane and doped-decane respectively. The 3D tomograms were recorded at the same locations (where tomograms were recorded after drainage) with

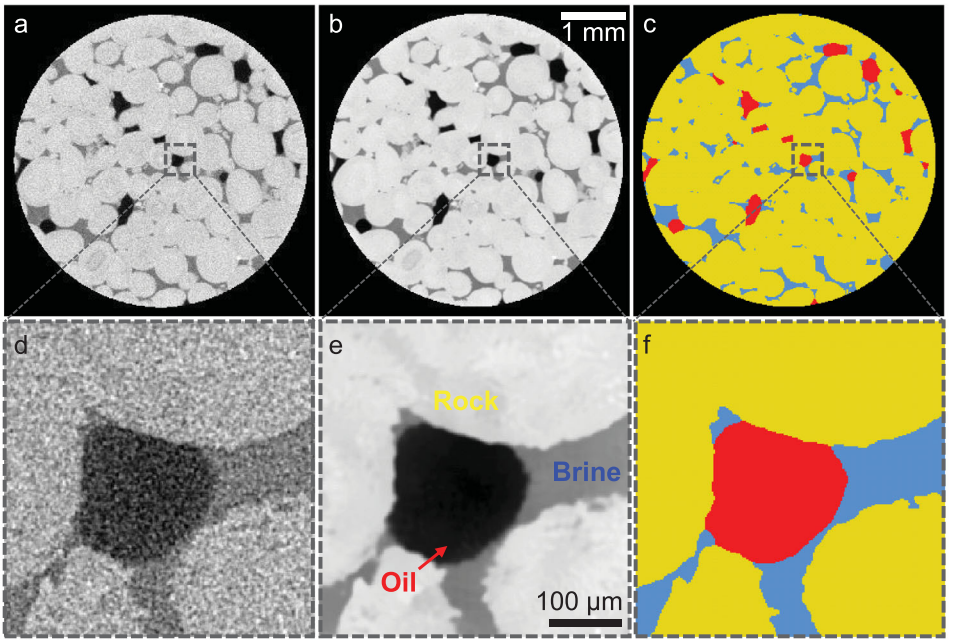

Figure 2. Image processing and segmentation. (a) Two-dimensional horizontal cross section of a raw tomographic image with a voxel size of 6.4 μm. Here, black, grey and light grey represent oil, brine and Ketton rock respectively. (b) The data set was then filtered using nonlocal means edge preserving filter. (c) The filtered image was segmented into three phases using watershed algorithm. Here, red, blue and yellow represent oil, brine and Ketton rock respectively. (d–f) Zoomed up sections of high-resolution images (voxel size = 2 μm).

a voxel size of 6.4 μm (1400–2400 projections) for phase saturations, curvature analysis and pore-throat partitioning. For water-wet and mixed-wet studies of contact angle and oil layer thickness, tomograms were acquired with a voxel size of 2 μm (2800 projections) and 2.5 μm (2200 projections) respectively.

For the mixed-wet experiment, the sample was further flushed with the brine for a total of 37 PV and tomograms were recorded with a voxel size of 6.4 μm, to observe the reduction in remaining oil saturation with subsequent brine injection.

2.3. Image Processing and Analysis

The tomograms were reconstructed using proprietary software provided by Zeiss and processed using Avizo-9 software unless otherwise specified. The tomograms were preprocessed to remove distorted outer regions and external walls (Figure 2a) and filtered with a nonlocal means edge preserving filter [*Buades et al*., 2005, 2008] (Figure 2b). Multiple tomograms recorded at different locations along the vertical axis were stitched together to obtain a total height of 10.7 mm, the center of which was at 10.5 mm from the base of the 25 mm rock sample. The total size of the complete image was 999 × 1018 × 1669 voxels and 1000 × 1020 × 1669 voxels for the water-wet and mixed-wet systems respectively. The tomograms were then segmented into three phases (solid, oil and brine) with a seeded watershed algorithm based on the grey-scale gradient and grey-scale intensity of each voxel (Figure 2c). A sensitivity analysis of the segmentation process was performed based on variation in intensity thresholds. The segmented data were analyzed for quantifying spatial distribution and volumes of each phase. The oil phase was isolated and each disconnected component was then labeled to perform cluster size distribution analysis as well as to visualize it in three dimensions. For brine-oil interfacial area measurements, first all the phase boundaries were detected, i.e., brine-oil, brine-rock and oil-rock. The brine-oil phase boundaries were then isolated from the rest. The interfacial area was calculated by measuring the area of the surface labeled as the brine-oil interface.

2.3.1. Contact Angle Measurement

The effective contact angle was estimated from higher resolution images (voxel size = 2 μm) using the method described in *Andrew et al*. [2014c]. First, the three-phase contact line was extracted from segmented data (Figure 3a), and it was then overlain on the filtered tomogram (Figure 3b). The filtered tomogram was realigned in the direction of red arrow in Figure 3b so that the image plane was perpendicular to

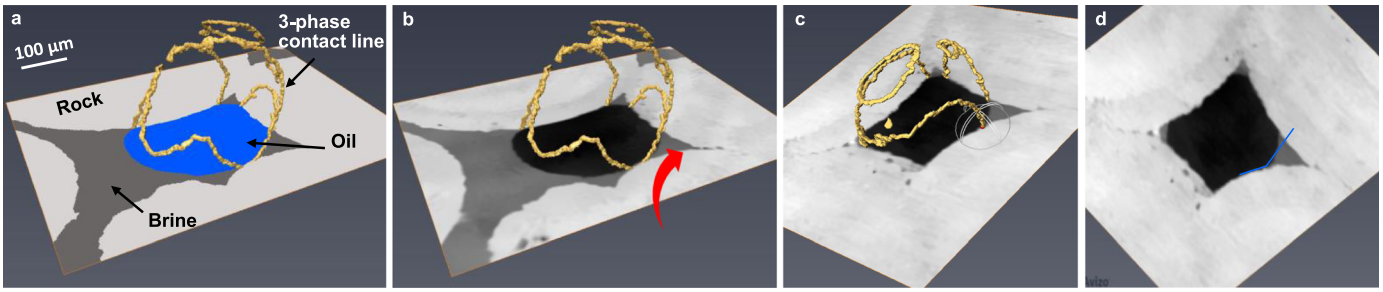

Figure 3. Contact angle estimation. (a) The segmented data were processed to identify three-phase contact line (yellow). (b) The extracted three-phase contact line was applied onto the filtered image. (c) The data were then realigned perpendicular to the contact line. The image was rotated in the direction of red arrow in Figure 3b to obtain a plane perpendicular to the contact line. (d) The contact angle was measured from the resampled image at the point where the plane was rotated.

the contact line (Figure 3c). The selection of the points for image realignment was made where the contact line was approximately straight to obtain a precise perpendicular plane. The image was then resampled and the contact angles were measured as shown in Figure 3d. The contact angle measurements were conducted at 100 locations randomly selected along the three-phase contact lines.

2.3.2. Brine-Oil Curvature Analysis

The brine-oil and the overall oil surface curvatures were obtained by creating best fit quadratic surfaces at each point on the smoothed surface generated from the segmented data [*Armstrong et al.*, 2012; *Andrew et al.*, 2014b]. Figure 4 shows the curvature mapping routine for an oil ganglion in a water-wet system. First, the curvature distribution of the oil in contact with the rest of the phases was obtained (Figures 4a and 4b), and then the oil-brine curvature was extracted by isolating the boundaries of brine-oil interface (Figures 4c and 4d). A Gaussian model using a trust region algorithm was fitted to the brine-oil distribution [*Conn et al.*, 2000]. In the case of a mixed-wet system, the brine-oil curvature was estimated on various subsets (of the segmented data) that were randomly selected at different locations along the height of the sample.

2.3.3. Pore-Throat Partitioning

The pore-throat partitioning workflow is shown in Figure 5. The pore space of the segmented image (Figures 5a and 5c) was isolated, which was then separated into individual pores by computing watershed basins on a Euclidian distance map of the pore-space (Figures 5b and 5d). The surfaces between individual pores were labeled as throats. The diameter of each pore and throat was obtained by calculating the diameter of the maximum inscribed sphere in that throat [*Dong and Blunt*, 2009]. Figure 5e shows the pore and throat size distribution of the Ketton rock sample that was used in the mixed-wet experiments.

For pore-throat partitioning of the brine invaded pore spaces after brine flooding, the invaded brine was isolated by subtracting the initial brine (obtained after drainage) from the total brine (obtained after brine flooding). The invaded brine image was then dilated by two voxels. The rock phase was then applied as a mask on this image. Pore-throat partitioning was then conducted on the resultant brine image. To obtain the throat size distribution of the oil-filled pore spaces after drainage, the oil was isolated from the image and the same image processing routine was applied.

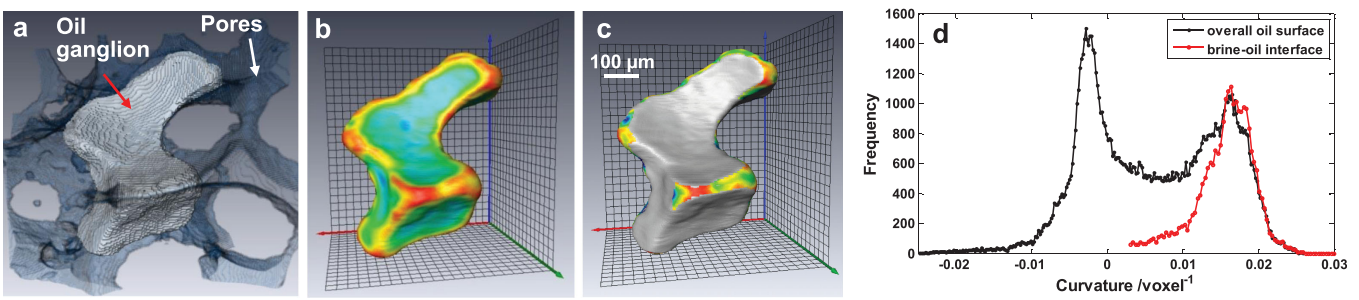

Figure 4. Curvature mapping. (a) The segmented oil ganglion (white) in the pore space (semitransparent grey). (b) Curvature of the ganglion obtained by creating best fit quadratic surfaces from the voxelized image. (c) Curvature of brine-oil interface which was isolated from the oil-rock interfaces. (d) Histograms of the curvature measurements of Figures 4b and 4c shown in black and red respectively.

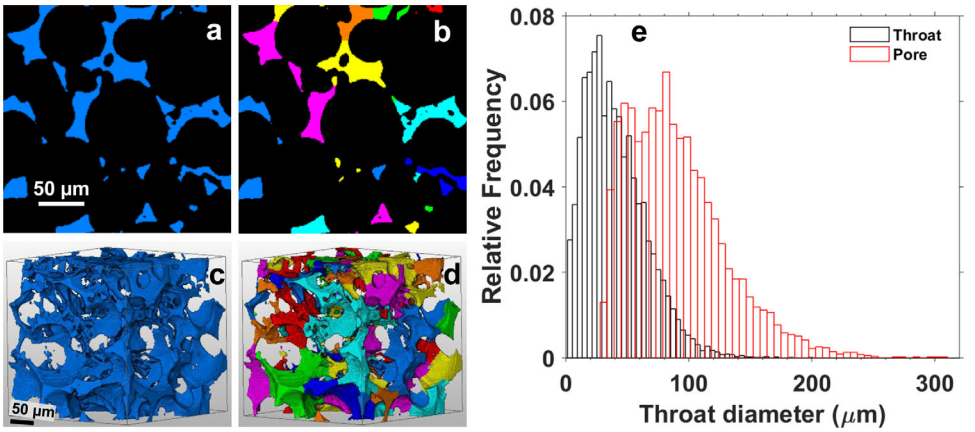

Figure 5. Pore-throat partitioning. (a) Two-dimensional cross section of a two-phase segmented subset of the tomogram with pore space (blue) and rock (black). (b) The pore space was isolated and partitioned into pores and throats. (c) and (d) show the three-dimensional rendering of Figures 5a and 5b. The rest of the phases are transparent. The different colors in (d) represent individual pores. The interfaces between individual pores were labeled as throats. (e) The pore (red) and throat (black) size distributions of the Ketton rock sample used in the mixed-wet experiments. The pore-throat partitioning analysis was conducted on tomograms with a voxel size of 6.4 μm.

3. Results and Discussion

3.1. Oil Morphologies in Mixed-Wet Systems

3.1.1. Oil Morphology After Primary Oil Injection in Mixed-Wet Systems

Figure 6a shows a two-dimensional vertical cross section of the reconstructed tomogram after oil flooding. Three-dimensional rendering of the oil phase (Figure 6b) shows a well-connected percolating oil cluster (blue) with a few isolated oil ganglia (shown in different colors), as observed in previous work imaging fluid distributions after primary drainage [*Roof*, 1970; *Berg et al*., 2013]. From the analysis of the segmented tomograms (low-resolution data with a voxel size of 6.4μm), we obtained an initial oil fraction of 0.594 $\pm$ 0.009, of which 96.7% is contributed by the largest percolating cluster. Figure 6c shows the brine-oil (connected oil) curvature distribution of various subsets (SS1–SS6). An example of the three-dimensional curvature maps of a subset SS5 is shown in Figure 6d. A positive brine-oil curvature distribution confirms the nonwetting oil conditions obtained during oil injection. The fitted peak positions of the curvature distributions range from 0.0183 μm^{-1} to 0.024 μm^{-1} (corresponding to a capillary pressure of about 491 Pa to 644 Pa), with most of them close to 0.022 μm^{-1}, corresponding to a capillary pressure of 590 Pa. For capillary-controlled displacement in equilibrium, all the interfaces of the connected oil cluster have equal curvatures; however, the limited imaging resolution and noise in the tomograms may be the reason for the small variation in the measurements.

3.1.2. Oil Morphology After Brine Injection in Mixed-Wet Systems

After 19 pore volumes of brine injection, the oil recovery in the mixed-wet case is found to be 73.8% of the original oil volume, corresponding to a remaining oil saturation of 0.152 $\pm$ 0.004. Further injection of brine up to 37 pore volumes reduced the oil saturation slightly to 0.147 $\pm$ 0.005, which indicates that there is a slow drainage of oil from the system. These values are close to the residual saturation of 0.188 obtained by Iglauer et al. [2012] using crude oil after 10 pore volumes of brine injection into a Clashach sandstone sample. By contrast, *Kumar et al*. [2010] obtained a higher value of residual saturation 0.346 after 7–10 pore volumes of brine injection into a sucrosic dolomite sample, which is even larger than that obtained in their strongly water-wet system (0.286). The possible reason for their higher residual saturation in the mixed-wet system could be due to the patched wettability that was created before conducting drainage and waterflooding experiments. The patched-wetting conditions in the rock might have led to unstable oil layers and their rupture, and therefore leading toward the trapping of significant amount of oil after brine injection.

The distribution of oil in the pore space after 19 pore volumes of brine injection is shown in Figures 7a and 7b. The remaining oil forms thin sheet-like structures, as observed previously by Iglauer et al. [2012]. The colors in the image represent disconnected portions of the oil phase. However, a careful slice-by-slice inspection of the high-resolution tomogram with a voxel size of 2.5 μm, which was captured at 2.5 mm from the sides (xy) and 3.2 mm from the base (z) of the larger imaged volume, shows that the oil is

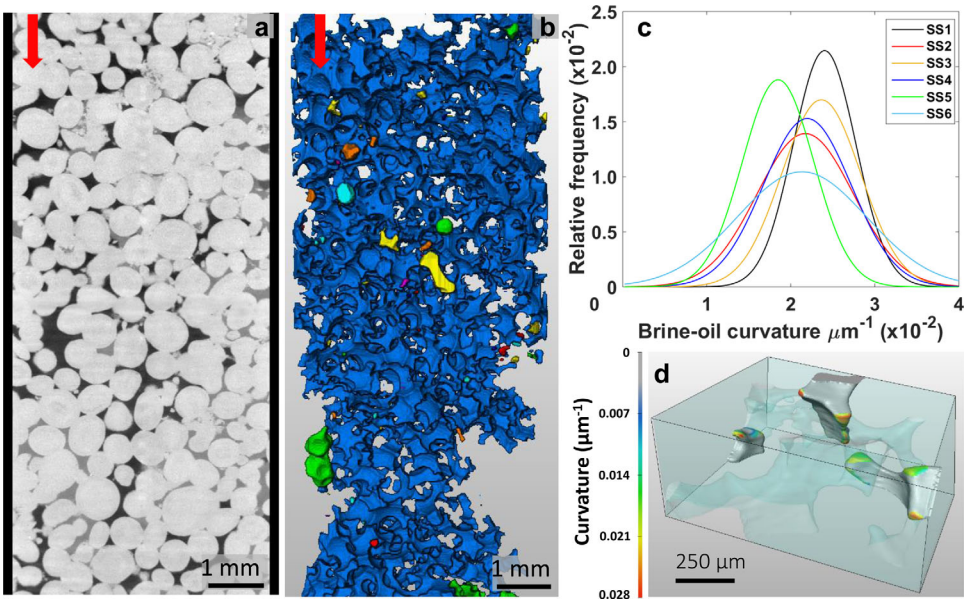

Figure 6. Primary oil injection in a mixed-wet system. (a) Two-dimensional vertical cross sections of a filtered tomographic image. Here, black, grey and dark grey color represent oil, rock and brine respectively. (b) Three-dimensional rendering of the oil phase. Brine and rock are transparent for effective visualization. The arrows indicate the direction of flow. Blue represents the connected oil cluster, while other colors represent disconnected oil clusters. (c) A plot of the Gaussian fit to the brine-oil interface curvature distributions of the connected oil cluster. SS1–SS6 represent small subsets of the connected oil cluster at different locations. (d) An example of the curvature maps (three-dimensional surface view) of the brine-oil interfaces of SS5. Here blue represents low curvatures while red represents high curvatures. Oil-rock contact regions are shown in grey, which were ignored in this analysis. Brine and rock surfaces are rendered transparent and semi-transparent respectively for effective visualization. The data analysis was performed on 6.4 μm voxel size tomograms.

connected throughout the imaging window in the form of thin oil layers located in the pore corners and sandwiched between two brine interfaces which are not resolved in the lower resolution image. This is further discussed in the later part of this section and explained in Figure 8. Based on the qualitative analysis from the high-resolution image, we hypothesize that the oil layers are connected throughout the porous medium, which could provide a conductive path for slow oil drainage with further injection of brine.

From the analysis of ten equal subsets (999 × 1018 × 337 voxels) created along the height of the sample, we observe a lower initial oil saturation (S_{oi}) near the base of the image which resulted in a lower remaining oil saturation (S_{orem}) at the base after brine injection. This is shown in Figure 7c. The porosity is nearly constant at all the locations. The variation in the trend in initial oil saturation particularly near the base is linked to the heterogeneity in the flow field during oil injection: Ketton limestone is known to have heterogeneous flow field as a result of pore-space heterogeneity [*Bijeljic et al.*, 2013]. The variation in the remaining oil saturation in the pore spaces after brine injection is explained by the throat size analysis in section 3.1.3. Figure 7d represents the remaining oil saturation as a function of initial oil saturation in subsets SS1–SS10. Except for the subset SS1 (at the base of the image), we observe an increasing trend in the remaining oil saturation with initial oil saturation up to about $S_{oi} = 0.5$, and then a decreasing trend with further increase in S_{oi}. This is similar to results on core samples reported in the literature which was explained in terms of the stability of oil layers [*Salathiel*, 1973; *Tanino and Blunt*, 2013].

Figure 8a shows a high-resolution image of the region where after brine flooding the oil appears to bulge into the brine. Comparing the same location at low-resolution, at the beginning of brine flooding, it is found that this brine-oil interface was established by primary drainage. Increasing the brine pressure during brine flooding did not appear to perturb the interface, which indicates that the brine cluster could be isolated from the rest of the brine. This could occur if the connected brine films and layers (molecular- to nano-scale [*Schmatz et al.*, 2015]) rupture during wettability alteration [*Blunt*, 1997] leaving a disconnected brine cluster/pool surrounded by oil. We have identified six such locations in the sample where the brine was isolated, by conducting label analysis, i.e., labeling disconnected components of the brine phase in different colors.

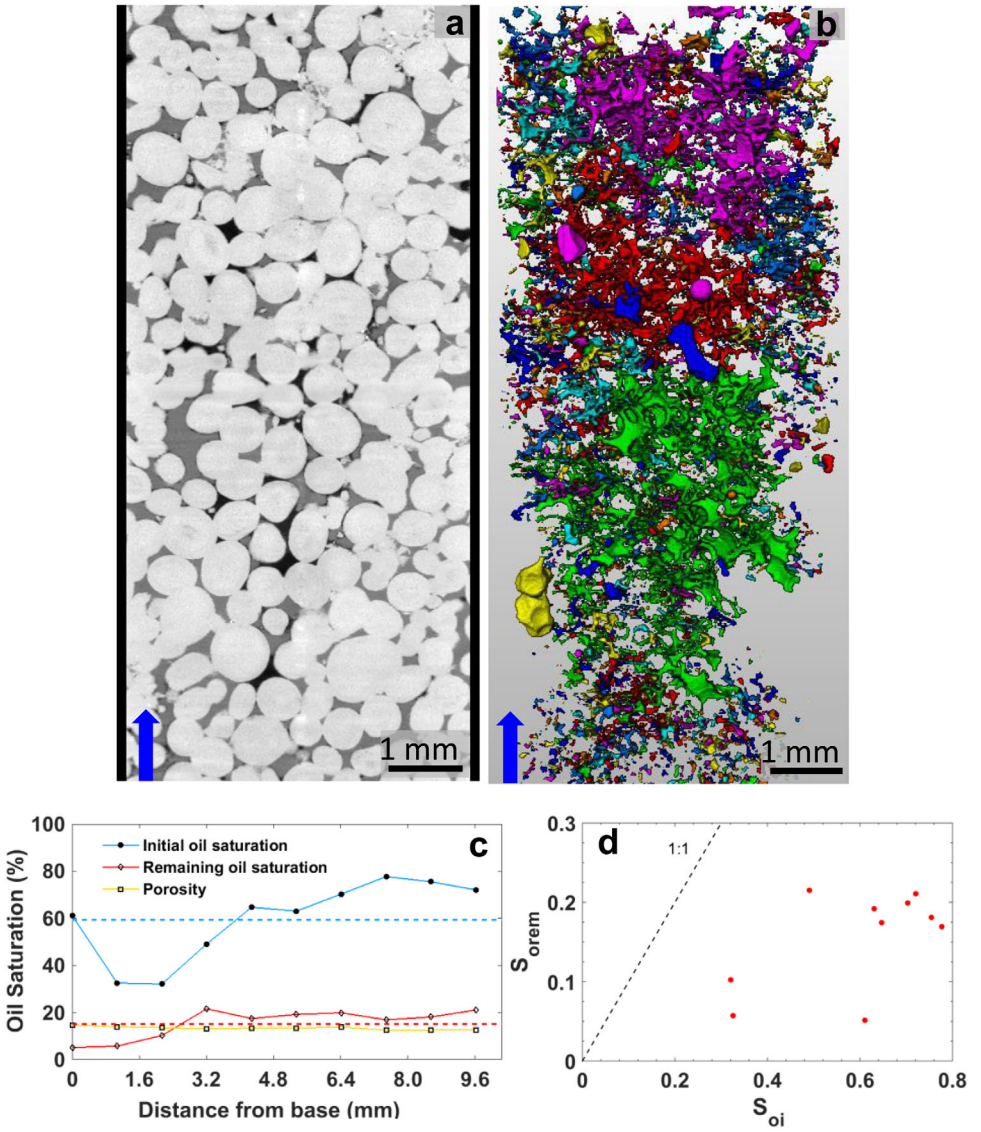

Figure 7. Brine flooding in a mixed-wet system. (a) Two-dimensional vertical cross section of the filtered tomogram after brine injection. Here, black, grey and dark grey represent oil, rock and brine respectively. (b) Three-dimensional rendering of the oil phase. The rest of the phases are transparent for effective visualization. The different colors represent disconnected components of the oil phase. (c) Vertical subsets along the height analyzed for porosity and initial and remaining oil saturation. Dashed blue and red lines represent the overall initial and remaining oil saturation in the complete tomogram respectively. (d) A plot of remaining oil saturation as a function of initial oil saturation in various subsets along the height of the sample. The data analysis was performed on 6.4 μm voxel size tomograms.

Figure 8b shows a location where the brine invaded the oil-wet pores. The shape of the brine-oil interface here clearly shows strong nonwetting brine conditions with a contact angle $\theta=180°$ (measured through the brine phase). There appears to be a wetting oil film separating the brine and the rock surface. These films are absent where the initial brine was in place after oil flooding (compare with Figure 8a). The brine invades the middle of the pore space leaving behind oil layers, by which we mean thicker structures where oil collects in the pore corners. These oil layers can also exist between two brine interfaces. This can be seen in Figure 8c where the oil layer was sandwiched between initial brine (without oil films) and the invading brine.

Figures 8d–8g show an example image of the pore space where such sandwiched and corner oil layers are formed in oil-wet portions of the mixed-wet system. The rock is rendered semitransparent for the effective visualization of the liquids (Figure 8d). The oil (yellow) as a nonwetting phase invades the larger pores initially filled with brine (blue) during oil injection (Figure 8e). After ageing, the wettability of the oil-filled

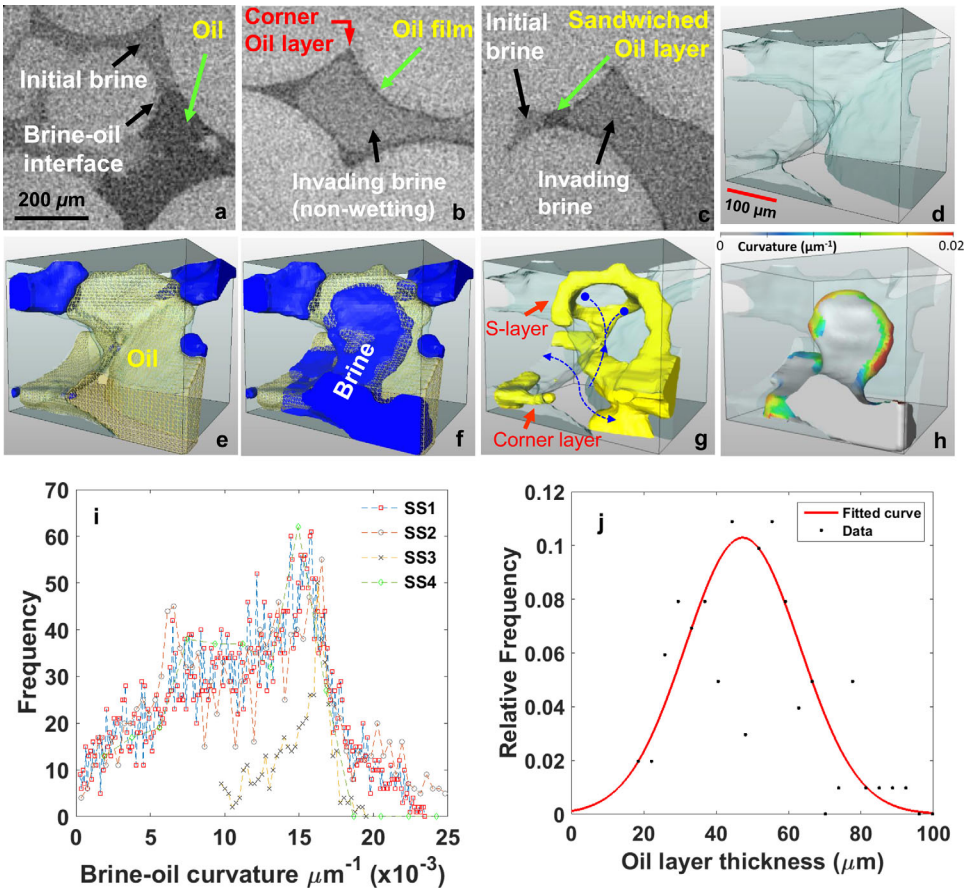

Figure 8. Oil layer formation in a mixed-wet system. (a) Interfacial curvature between brine and oil. Here black, dark grey and grey represent oil, brine and rock respectively. Here the oil appears to bulge into the brine, indicating a local positive capillary pressure. (b) Brine invasion into an oil-wet pore with θ=180°. Oil layers in the pore corners are clearly visible. Oil also stays as thin films between the brine and the rock surfaces. (c) An oil layer sandwiched between initial brine and the invading brine. Figures 8a–8c were acquired at high-resolution with a voxel size of 2.5 μm. (d–g) The process of brine invasion and oil layer formation in a wettability altered (oil-wet) pore of a mixed-wet system. Here, the rock is rendered semitransparent. (d) Rock surfaces (semitransparent) and pore spaces (transparent). (e) The pore-scale distribution of fluids after oil flooding. Brine and oil are shown in blue and yellow respectively. (f and g) The same pore after brine flooding. After ageing, the surfaces in contact with oil (in Figure 8e) altered their wettability to oil-wet. Brine as the nonwetting phase invaded the center of the pore (Figure 8f) leaving oil (yellow) as wetting layers in the corners and sandwiched (S-layer) between brine interfaces (Figure 8g). Dashed blue arrows indicate the direction of brine invasion. (h) Brine-oil curvature maps of the invaded brine. Blue represents low curvatures while red represents high curvatures. (i) The plot of curvature distribution of four different subsets. The analysis in Figures 8d–8i was conducted on low-resolution images (voxel size = 6.4 μm). (j) Oil layer thickness distribution estimated from the high-resolution filtered tomogram (voxel size = 2.5 μm).

portion of the pore space changes to oil-wet. During brine injection, the brine invades the center of the oil-wet pore spaces as a nonwetting phase (Figure 8f), leaving wetting layers of oil (yellow) in pore corners and sandwiched between two brine interfaces, e.g., marked by red arrows (Figure 8g). Our measurements indicate that the thickness of these oil layers, which was measured from the two-dimensional cross sections of the high-resolution raw tomogram (voxel size = 2.5 μm), can extend up to 109 μm, with an average value of 47 $\pm$ 17 μm. A histogram of the oil layer thickness is shown in Figure 8j. The oil layers in this example image are connected which is consistent with the observation from the high-resolution raw images. This gives us a confidence to hypothesize that they are connected throughout the pore space, even if this was not captured in the low resolution images. Oil can slowly drain through these layers, resulting in lower oil saturation after many pore volumes of brine injection. We see the effect of the layer flow where the oil saturation decreased from 0.152 to 0.147 with 18 pore volumes of brine injection, indicating the low but finite conductivity of the oil phase. The oil layers are expected to reduce in size and eventually rupture with decreasing capillary pressure (increasing brine pressure) [*van Dijke and Sorbie*, 2006; *Ryazanov et al*., 2014].

The curvature map of the invading brine in the pore space presented in Figure 8d is shown in Figures 8h and 8i. A positive curvature with respect to the brine phase indicates that the brine invades the oil-wet pore

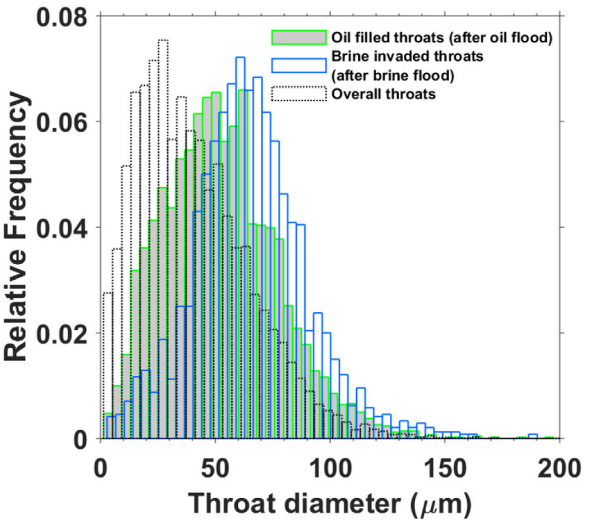

Figure 9. Throat invasion analysis in a mixed-wet system. The overall throat size distribution is shown in dotted-black. Oil filled throats after oil flood are indicated by green bars. After brine flood, the throats (initially filled with oil) invaded by brine are marked in blue.

space as a nonwetting phase. The peak position of the measured curvatures in these subsets is 0.01588 ± 0.0007 μm^{-1}, corresponding to a capillary pressure of -425.9 ± 18.8 Pa: the negative values indicate that the brine pressure is higher than the oil pressure. These curvatures are measured at the static interfaces after the conclusion of a brine flood.

3.1.3. Pore-Throat Invasion During Oil and Brine Injection in Mixed-Wet Systems

The throat size distribution of the oil-invaded pore spaces after oil injection is shown in Figure 9 (green bars), with a mean value of 52.4 μm. The size distribution of oil-invaded throats covers the right hand side of the overall throat size distribution (with a mean value of 40.32 μm) shown in dotted-black (also in Figure 5e), which indicates that the oil as a nonwetting phase invades through larger throats during drainage.

The size distribution of brine-invaded throats (initially filled with oil) after brine injection (blue bars), with a mean value of 65.31 μm, covers the right hand side of the oil-filled throat distribution curve (green bars). From this analysis, it is clear that the brine as a nonwetting phase invades only the larger available oil-wet throats during brine injection, and smaller throats remain oil filled, since they require a lower (more negative) capillary entry pressure to fill.

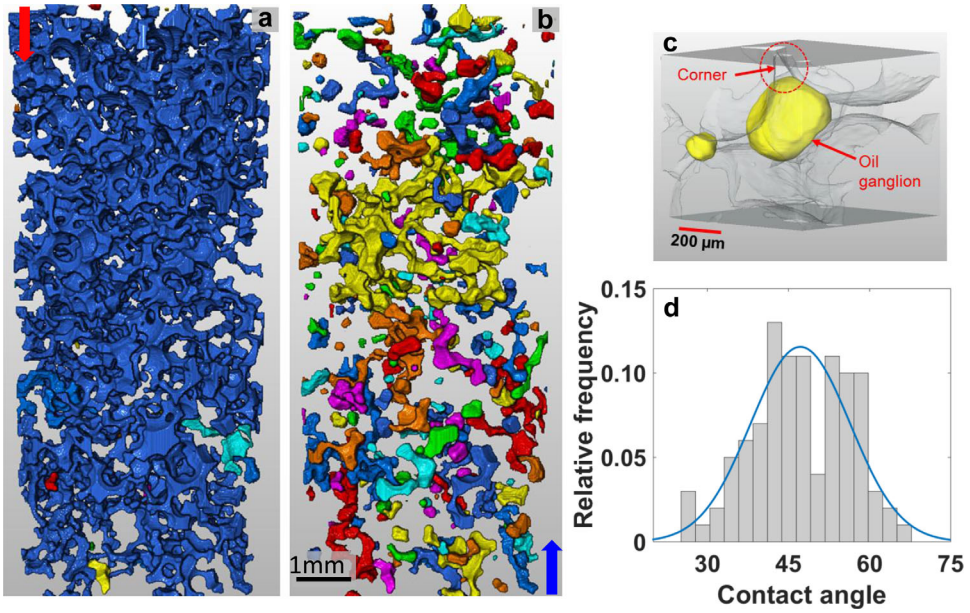

Figure 10. Water-wet system. (a) and (b) Three-dimensional renderings of the oil phase after oil and brine injection respectively. Brine and rock phases are transparent for effective visualization. The arrows marked on the images indicate the direction of flow during fluid injection. Different colors represent disconnected oil ganglia. (c) Volume rendering of oil ganglia (yellow) trapped in single pore bodies. The rock is rendered semitransparent and brine transparent for effective visualization. It is clear that in a water-wet system, the trapped ganglia occupy the centers of the pores while the corners are filled with brine. (d) Equilibrium contact angle distribution obtained from three-dimensional tomograms. The mean of the distribution is 47°, indicating weakly water-wetting conditions. Figures 10a–10c were produced from low-resolution tomograms (voxel size = 6.4 μm), while the contact angle analysis in Figure 10d was conducted on high-resolution tomograms (voxel size = 2 μm).

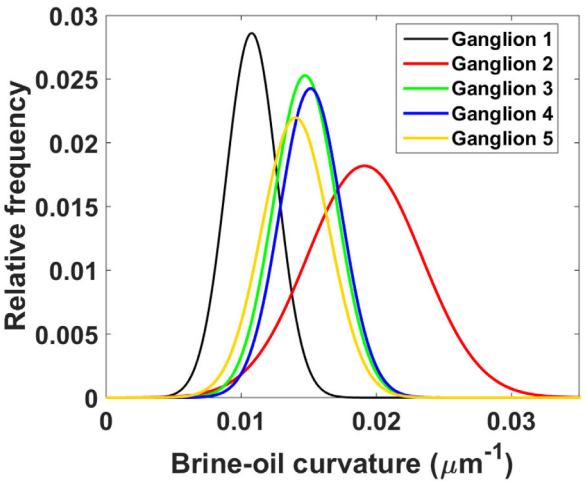

Figure 11. Brine-oil curvature distribution of disconnected oil ganglia after brine injection in a water-wet system. The analysis was performed on tomograms with a voxel size of 6.4 μm.

3.2. Oil Morphologies in Water-Wet Systems and Comparison With Mixed-Wet Systems

For the case of a water-wet system, the initial oil after 16 pore volumes of oil injection formed a connected percolating oil cluster (blue) as shown in Figure 10a. The initial oil saturation was found to be 0.59 ± 0.004. Both findings (quantitative and qualitative) for the water-wet case are similar to those obtained for the mixed-wet system after oil flood presented in section 3.1.1 and Figure 6b, which guarantees us a fair comparison of both systems after brine injection under different wetting conditions.

Figure 10b shows the volume rendering of the residual oil after 18.5 pore volumes of brine injection in a water-wet system. The residual oil forms disconnected ganglia, shown in different colors, occupying single to multipore bodies. The oil ganglia reside in the centers of the larger pores while the brine occupies the smaller pores and pore corners as shown in Figure 10c. This is different from that obtained for a mixed-wet system in which connected oil layers, either in pore corners or sandwiched between two brine interfaces, were observed throughout the porous medium (compare with Figure 8g). The final residual oil saturation in the water-wet system is found to be 0.272 ± 0.005. Although the oil saturation is about a factor of two larger than that obtained in the mixed-wet system under similar flow conditions, our experimentally measured brine-oil interfacial area per unit volume of the porous medium (estimated from the image analysis) is about a factor of three smaller than that measured for the mixed-wet system, $3.92 \times 10^{-4}\ \mu m^{-1}$ compared to $11.63 \times 10^{-4}\ \mu m^{-1}$, indicating a more compact morphology of the trapped clusters and a lower potential for dissolution in water-wet systems.

3.2.1. In Situ Contact Angle Measurements in Water-Wet Systems

The equilibrium contact angle at the three-phase contact line was estimated from higher resolution images (voxel size = 2 μm). A histogram of the contact angle distribution and its Gaussian fit is shown in Figure 10d which gives a mean value of the contact angle $\theta = 47 \pm 9°$ (measured through the brine), indicating a weakly water-wet system, similar to the values measured on the same rock for a CO_2-brine system at 50°C and 10 MPa [*Andrew et al.*, 2014c].

3.2.2. Curvature and Capillary Pressure of Disconnected Oil Clusters

Here we measure the curvature distribution and capillary pressure of oil clusters in water-wet systems and compare it with mixed-wet systems results presented in section 3.1.2. Figure 11 shows the curvature distribution of five ganglia after brine injection in water-wet systems. The fitted curvature peaks show a broad range from 0.01 ± 0.002 to 0.02 ± 0.002 corresponding to a capillary pressure in the range 0.86 ± 0.171 kPa to 1.53 ± 0.196 kPa. All these pressures are positive, indicative of oil being the nonwetting phase; in contrast for the mixed-wet systems, the curvature of the fluid-fluid interfaces had the opposite sign with a negative capillary pressure. The curvature values span those measured for the mixed-wet system, indicating that we are accessing pores of similar size in both cases: the higher capillary pressure for the water-wet system is due to the higher interfacial tension in these experiments. The reason for the large variation in the capillary pressure of the disconnected ganglia is that the ganglion preserves the capillary pressure at which it becomes disconnected during brine injection. The local capillary pressure estimated from the image analysis provides us the information about the time at which ganglion was disconnected during fluid flow, which cannot be predicted from the measurements of macroscopic capillary pressure. This contrasts with the mixed-wet system, where the curvature is approximately constant, indicating a connected oil phase in capillary equilibrium.

4. Conclusions

This study provides a fundamental understanding of the pore-scale entrapment of oil and oil layer formation as a function of the wettability of the porous medium. We have used X-ray micro-tomography to

investigate fluid distribution, in situ contact angles, pore-scale (local) capillary pressure estimation and pore-throat analysis after sequential oil and brine injection in a carbonate rock under two wettability regimes. The wettability of the rock was altered in situ by using fatty acid doped in the oil phase during oil injection which resulted in strongly oil-wet conditions (contact angle, $\theta = 180^{\circ}$) in the oil-filled pore spaces.

For mixed-wet systems, we performed throat invasion analysis in both oil and brine flooding, and related the fluid occupancy to the throat size. Our analysis indicates that the brine (during brine flooding) invades only the larger available oil-wet throats, while smaller throats remain oil-filled, since they require a lower (more negative) capillary entry pressure to fill.

The formation of oil layers during brine flooding in a mixed-wet system has been hypothesized in the literature and included in many theoretical and modeling studies. We provide experimental evidence of the existence of such connected oil layers in oil-wet pore corners of a mixed-wet system; the thickness of these layers extend up to 109 μm with an average value of 47 ± 17 μm. The decrease in the remaining oil saturation (from 0.152 ± 0.004 to 0.147 ± 0.005) with 18 pore volumes of brine injection (from 19 to 37 pore-volume injection) indicates the slow conductance of oil through these layers. The connectedness of these layers is also evident from the fact that the brine-oil curvature distribution is constant at different locations throughout the rock. This is in contrast to that obtained for disconnected oil ganglia in a water-wet system, which preserve the capillary pressure of the throat at which they become disconnected. The oil layers that are formed under strongly wet conditions ($\theta = 180^{\circ}$) are stable under our experimental flow conditions. Further research could focus on investigating the stability of oil layers as a function of contact angle and capillary pressure in mixed-wet rocks.

Acknowledgments

We gratefully acknowledge funding from the Qatar Carbonates and Carbon Storage Research Centre (QCCSRC), provided jointly by Qatar Petroleum, Shell, and Qatar Science & Technology Park. The authors gratefully acknowledge Marry Raj Karappillil for her help in contact angle measurements, and Ali Raeini for his help in pore-throat analysis. The authors thank the three anonymous reviewers for their valuable comments and suggestions. The data acquired are available from the corresponding author.

References

Al-Raoush, R. I. (2009), Impact of wettability on pore-scale characteristics of residual nonaqueous phase liquids, *Environ. Sci. Technol.*, *43*(13), 4796–4801.

Andreas, J. M., E. A. Hauser and W. B. Tucker (1937), Boundary tension by pendant drops, *J. Phys. Chem.*, *42*(8), 1001–1019.

Andrew, M., B. Bijeljic, and M. J. Blunt (2014a), Pore-scale imaging of trapped supercritical carbon dioxide in sandstones and carbonates, *Int. J. Greenhouse Gas Control*, *22*, 1–14.

Andrew, M., B. Bijeljic and M. J. Blunt (2014b), Pore-by-pore capillary pressure measurements using X-ray microtomography at reservoir conditions: Curvature, snap-off, and remobilization of residual CO_2, *Water Resour. Res.*, *50*, 8760–8774, doi:10.1002/2014WR015970.

Andrew, M., B. Bijeljic and M. J. Blunt (2014c), Pore-scale contact angle measurements at reservoir conditions using X-ray microtomography, *Adv. Water Resour.*, *68*, 24–31.

Andrew, M., H. Menke, M. Blunt and B. Bijeljic (2015), The imaging of dynamic multiphase fluid flow using synchrotron-based X-ray microtomography at reservoir conditions, *Transp. Porous Media*, *110*(1), 1–24.

Armstrong, R. T., M. L. Porter, and D. Wildenschild (2012), Linking pore-scale interfacial curvature to column-scale capillary pressure, *Adv. Water Resour.*, *46*, 55–62.

Berg, S., et al. (2013), Real-time 3D imaging of Haines jumps in porous media flow, *Proc. Natl. Acad. Sci. U. S. A.*, *110*(10), 3755–3759.

Bijeljic, B., P. Mostaghimi, and M. J. Blunt (2013), Insights into non-Fickian solute transport in carbonates, *Water Resour. Res.*, *49*, 2714–2728, doi:10.1002/wrcr.20238.

Blunt, M. J. (1997), Pore level modeling of the effects of wettability, *Soc. Pet. Eng. J.*, *2*(4), 494–510.

Blunt, M. J. (2001), Flow in porous media—Pore-network models and multiphase flow, *Curr. Opin. Colloid Interface Sci.*, *6*(3), 197–207.

Buades, A., B. Coll, and J. M. Morel (2005), A non-local algorithm for image denoising, *IEEE Comput. Soc. Conf. Comput. Vision Pattern Recognition*, *2*, 60–65.

Buades, A., B. Coll, and J.-M. Morel (2008), Nonlocal image and movie denoising, *Int. J. Comput. Vision*, *76*(2), 123–139.

Chatzis, I., N. R. Morrow and H. T. Lim (1983), Magnitude and detailed structure of residual oil saturation, *SPEJ Soc. Pet. Eng. J.*, *23*(2), 311–326.

Cieplak, M., and M. O. Robbins (1988), Dynamical transition in quasistatic fluid invasion in porous media, *Phys. Rev. Lett.*, *60*(20), 2042–2045.

Cieplak, M., and M. O. Robbins (1990), Influence of contact angle on quasistatic fluid invasion of porous media, *Phys. Rev. B*, *41*(16), 11508–11521.

Conn, A. R., N. I. M. Gould and P. L. Toint (2000), *Trust Region Methods*, Society for Industrial and Applied Mathematics (SIAM), Philadelphia, Pa.

Dong, H., and M. J. Blunt (2009), Pore-network extraction from micro-computerized-tomography images, *Phys. Rev. E*, *80*(3), 036307.

Feali, M., W. V. Pinczewski, Y. Cinar, C. H. Arns, J.-Y. Arns, M. Turner, T. Senden, N. Francois, and M. A. Knackstedt (2012), Qualitative and quantitative analyses of the three-phase distribution of oil, water, and gas in bentheimer sandstone by use of micro-ct imaging, *SPE Reservoir Eval. Eng.*, *15*(6), 706–711.

Goebel, A., and K. Lunkenheimer (1997), Interfacial tension of water/n-alkane interface, *Langmuir*, *13*, 369–372.

Hamouda, A. A., and K. A. Rezaei Gomari (2006), *Influence of Temperature on Wettability Alteration of Carbonate Reservoirs*, in *SPE/DOE Symposium on Improved Oil Recovery*, Tulsa, Okla., 22–26 April 2006, 99848, pp. 1–12.

Hansen, G., A. A. Hamouda and R. Denoyel (2000), The effect of pressure on contact angles and wettability in the mica/water/n-decane system and the calcite+stearic acid/water/n-decane system, *Colloids Surf. A*, *172*(1–3), 7–16.

Honeyman, B. D. (1999), Geochemistry: Colloidal culprits in contamination, *Nature*, *397*(6714), 23–24.

Iglauer, S., S. Favretto, G. Spinelli, G. Schena, and M. J. Blunt (2010), X-ray tomography measurements of power-law cluster size distributions for the nonwetting phase in sandstones, *Phys. Rev. E*, *82*(5), 056315.

Iglauer, S., M. A. Fernø, P. Shearing, and M. J. Blunt (2012), Comparison of residual oil cluster size distribution, morphology and saturation in oil-wet and water-wet sandstone, *J. Colloid Interface Sci.*, *375*(1), 187–192.

Kovscek, A. R., H. Wong, and C. J. Radke (1993), A pore-level scenario for the development of mixed wettability in oil reservoirs, *AIChE J.*, *39*(6), 1072–1085.

Kumar, M., M. A. Knackstedt, T. J. Senden, A. P. Sheppard and J. P. Middleton (2010), Visualizing and quantifying the residual phase distribution in core material, *Petrophysics*, *51*(5), 323–332.

Morrow, N., and J. Buckley (2011), Improved oil recovery by low-salinity waterflooding, *J. Pet. Technol.*, *65*(05), 106–112.

Pak, T., I. B. Butler, S. Geiger, M. I. J. van Dijke, and K. S. Sorbie (2015), Droplet fragmentation: 3D imaging of a previously unidentified pore-scale process during multiphase flow in porous media, *Proc. Natl. Acad. Sci. U. S. A.*, *112*(7), 1947–1952.

Piri, M., and M. J. Blunt (2005), Three-dimensional mixed-wet random pore-scale network modeling of two- and three-phase flow in porous media. I. Model description, *Phys. Rev. E*, *71*(2), 026301.

Roof, J. G. (1970), Snap-off of oil droplets in water-wet pores, *Soc. Pet. Eng. J.*, *10*(1), 85–90.

Ryazanov, A. V., M. I. J. Van Dijke, and K. S. Sorbie (2010), Pore-network prediction of residual oil saturation based on oil layer drainage in mixed-wet systems, in *Proceedings of SPE Symposium on Improved Oil Recovery*, vol. 2, pp. 1217–1232, Curran Associates, Inc., Tulsa, Okla., 24–28 April 2010.

Ryazanov, A. V., K. S. Sorbie and M. I. J. van Dijke (2014), Structure of residual oil as a function of wettability using pore-network modelling, *Adv. Water Resour.*, *63*, 11–21.

Salathiel, R. A. (1973), Oil recovery by surface film drainage in mixed-wettability rocks, *J. Pet. Technol.*, *25*(10), 1216–1224.

Schmatz, J., J. L. Urai, S. Berg, and H. Ott (2015), Nanoscale imaging of pore-scale fluid-fluid-solid contacts in sandstone, *Geophys. Res. Lett.*, *42*, 2189–2195, doi:10.1002/2015GL063354.

Schnaar, G., and M. L. Brusseau (2005), Pore-Scale characterization of organic immiscible-liquid morphology in natural porous media using synchrotron x-ray microtomography, *Environ. Sci. Technol.*, *39*(21), 8403–8410.

Shaffer, G. (2010), Long-term effectiveness and consequences of carbon dioxide sequestration, *Nat. Geosci.*, *3*(7), 464–467.

Singh, K., R. K. Niven, T. J. Senden, M. L. Turner, A. P. Sheppard, J. P. Middleton, and M. A. Knackstedt (2011), Remobilization of residual non-aqueous phase liquid in porous media by freeze−thaw cycles, *Environ. Sci. Technol.*, *45*(8), 3473–3478.

Stauffer, C. E. (1965), The measurement of surface tension by the pendant drop technique, *J. Phys. Chem.*, *69*(6), 1933–1938.

Tanino, Y., and M. J. Blunt (2013), Laboratory investigation of capillary trapping under mixed-wet conditions, *Water Resour. Res.*, *49*, 4311–4319, doi:10.1002/wrcr.20344.

Trojer, M., M. L. Szulczewski, and R. Juanes (2015), Stabilizing fluid-fluid displacements in porous media through wettability alteration, *Phys. Rev. Appl.*, *3*(5), 054008.

Valvatne, P. H., and M. J. Blunt (2004), Predictive pore-scale modeling of two-phase flow in mixed wet media, *Water Resour. Res.*, *40*, W07406, doi:10.1029/2003WR002627.

van Dijke, M. I. J., and K. S. Sorbie (2006), Existence of fluid layers in the corners of a capillary with non-uniform wettability, *J. Colloid Interface Sci.*, *293*(2), 455–463.

Wildenschild, D., and A. P. Sheppard (2013), X-ray imaging and analysis techniques for quantifying pore-scale structure and processes in subsurface porous medium systems, *Adv. Water Resour.*, *51*, 217–246.